Pressure-driven Lifshitz transition in type-II Dirac semimetal $NiTe_2$

Mengyao Qi,[1,2] Chao An,[1] Yonghui Zhou,[2,*] Hao Wu,[2] Bowen Zhang,[2,3] Chunhua Chen,[2,3] Yifang Yuan,[2,3] Shuyang Wang,[2,3] Ying Zhou,[1] Xuliang Chen,[2] Ranran Zhang,[2] and Zhaorong Yang[1,2,4,†]

[1]*Institutes of Physical Science and Information Technology, Anhui University, Hefei 230601, China*

[2]*Anhui Province Key Laboratory of Condensed Matter Physics at Extreme Conditions, High Magnetic Field Laboratory, Chinese Academy of Sciences, Hefei 230031, China*

[3]*Science Island Branch of Graduate School, University of Science and Technology of China, Hefei 230026, China*

[4]*Collaborative Innovation Center of Advanced Microstructures, Nanjing University, Nanjing 210093, China*

(Received 16 December 2019; accepted 26 February 2020; published 16 March 2020)

Band engineering in layered transition metal dichalcogenides (TMDs) leads to a variety of emergent phenomena and has obtained considerable attention recently. Transition metal ditelluride $NiTe_2$ has been discovered experimentally to be a type-II Dirac semimetal at ambient pressure, and was predicted to display superconductivity in the monolayer limit. Here we systematically investigate the structural and electronic properties of type-II Dirac semimetal $NiTe_2$ under high pressure. Room-temperature synchrotron x-ray diffraction and Raman scattering measurements reveal the stability of the pristine hexagonal phase up to 52.2 GPa, whereas both the pressure coefficient and linewidth of Raman mode E_g exhibit anomalies at a critical pressure $P_c \sim 16$ GPa. Meantime, Hall resistivity measurement indicates that the hole-dominated behavior maintains up to 15.6 GPa and transforms into electron-dominated behavior at higher pressures. Our findings consistently demonstrate a pressure-induced Lifshitz transition in type-II Dirac semimetal $NiTe_2$.

DOI: 10.1103/PhysRevB.101.115124

Layered transition metal dichalcogenides (TMDs) have attracted extensive interest because of their rich physical properties [1–3] and potential applications in electronics and optoelectronics [4]. TMDs have a general formula MX_2 (M = transition metal; X = S, Se, or Te), where the adjacent X-M-X layers are held together by van der Waals interactions [5]. During the past several years, accompanied by exploration of novel topological electronic states, much attention has been paid to the TMDs focusing on their nontrivial band topology, leading to the theoretical prediction and experimental discovery of type-II Weyl semimetal in WTe_2 [6] and $MoTe_2$ [7], as well as type-II Dirac semimetal in $PtSe_2$ [8], $PdTe_2$ [9], and $PtTe_2$ [10]. Theoretically, the type-II Dirac (Weyl) semimetals possess highly tilted Dirac (Weyl) cones along certain momentum directions due to the violation of Lorentz invariance [6]. The linear energy dispersions of Dirac (Weyl) cones normally result in an ultrahigh carrier mobility and large nonsaturating magnetoresistance [11,12], rendering promising applications in electronics and spintronics. Very recently, $NiTe_2$ has been reported to be a type-II Dirac semimetal through quantum oscillation measurements and band structure calculations [13]. The topological feature in $NiTe_2$ has been further observed via spin- and angle-resolved photoemission spectroscopy [14]. It is found that the Dirac points of $NiTe_2$ are located just at ~0.02 eV above the Fermi level, more closely than its homologues $PdTe_2$ (0.5 eV) [15], $PtTe_2$ (0.8 eV) [10], and $PtSe_2$ (1.2 eV) [16], which may provide an advantageous platform to study the topological properties of the type-II Dirac semimetals [13,14]. More interestingly, based on *ab initio* calculations, it was predicted that monolayer $NiTe_2$ is an intrinsic superconductor with a critical temperature $T_c \sim 5.7$ K, while bilayer $NiTe_2$ intercalated with lithium displays a two-gap superconductivity with a $T_c \sim 11.3$ K [17].

As one of the fundamental state parameters, pressure has been proved to be an effective and clean way to tune the electronic states of TMDs according to the discoveries such as pressure-induced superconductivity, pressure-induced electronic topological transition (ETT), or Lifshitz transition, etc. [18–21]. In this work, we performed high-pressure x-ray diffraction (XRD), Raman scattering, and electrical transport measurements on type-II Dirac semimetal $NiTe_2$. With increasing pressure up to 71.2 GPa, although no traces of superconductivity have been detected down to 1.8 K, we demonstrate a Lifshitz transition instead. The Lifshitz transition, occurring around $P_c \sim 16$ GPa, is not only reflected in the anomalies of the pressure coefficient and linewidth of the Raman mode E_g, but also revealed by the sign change of the Hall coefficient.

Experimental details are presented in the Supplemental Material [22]. The synthesized $NiTe_2$ single crystals are characterized by the XRD and energy-dispersive x-ray spectroscopy (EDXS) experiments at ambient pressure. As illustrated in Supplemental Material, Fig. S1(a), bulk $NiTe_2$ crystallizes in the layered CdI_2-type structure with space group P-3m1 (No. 164). Figure S1(b) shows the XRD patterns of $NiTe_2$ single crystal. The observation of only (00l) diffraction peaks indicates a c-axis orientation of the as-grown crystals. Figure S1(c) displays the EDXS characterization,

*yhzhou@hmfl.ac.cn
†zryang@issp.ac.cn

 ©2020 American Physical Society

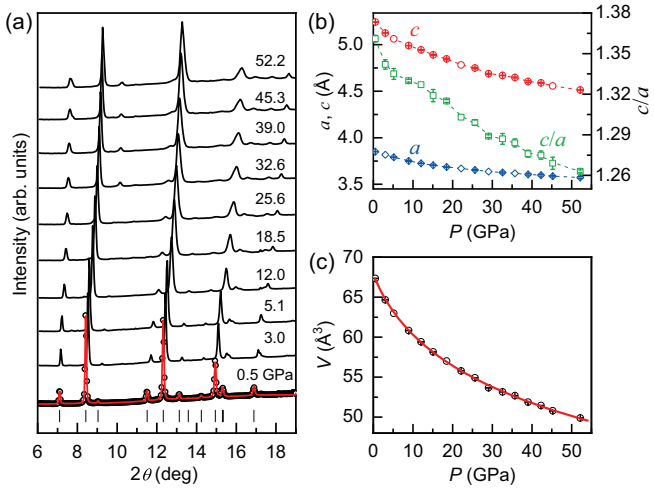

FIG. 1. High-pressure powder synchrotron XRD patterns of $NiTe_2$ at room temperature ($\lambda = 0.4133$ Å). (a) Representative diffraction patterns under compression up to 52.2 GPa. Le Bail refinement with a $P\text{-}3m1$ space group is shown for 0.5 GPa. The open circles and red line represent the observed and calculated data, respectively. The vertical bars indicate the position of Bragg peaks. (b) The pressure-dependent lattice parameters a and c, and axis ratio c/a. (c) Volume as a function of pressure. The open circles denote the data of the hexagonal ($P\text{-}3m1$, $Z = 1$) phase. The solid line is the fitting result based on the third-order Birch-Murnaghan equation of state.

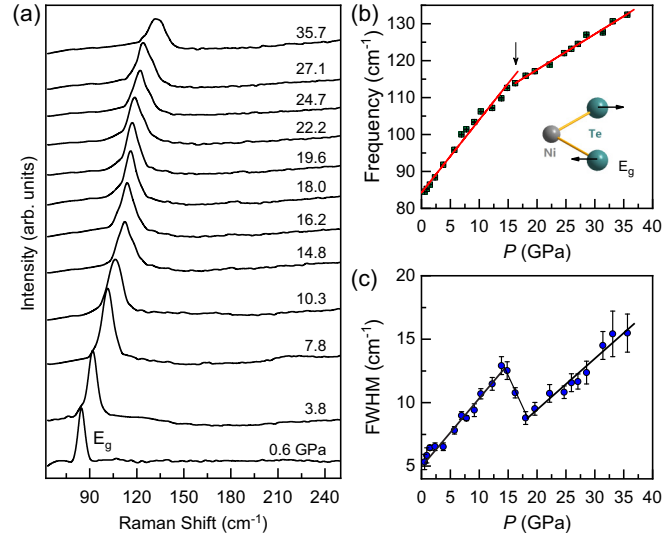

FIG. 2. (a) Pressure-dependent Raman spectra of $NiTe_2$ single crystal at room temperature. (b) The frequency of the E_g mode as a function of pressure. The red solid lines represent linear fittings. Inset: The schematic view of Raman mode E_g. (c) Pressure dependence of FWHM of the E_g mode. The black solid lines are guides to the eyes.

from which the real composition is determined to be $NiTe_{1.98}$. Powder XRD patterns confirm the pure hexagonal phase [see Fig. S1(d)]. The lattice parameters extracted via Le Bail fitting are $a = 3.8776$ Å, $c = 5.2653$ Å, in agreement with the previous report [13]. These results demonstrate the high quality of the sample used here.

To check the structural stability of pristine $NiTe_2$ under pressure, we performed high-pressure powder XRD measurements at room temperature. As shown in Fig. 1(a), all the XRD peaks continuously shift towards higher angles without new peaks appearing when the pressure increases up to 52.2 GPa, indicating the absence of structural phase transition in the pressurized $NiTe_2$. The XRD patterns under compression can be well indexed with the hexagonal $P\text{-}3m1$ phase in Le Bail refinements. A representative refinement of the XRD patterns at 0.5 GPa is presented at the bottom of Fig. 1(a). The fitting results of weighted profile factor R_{WP}, profile factor R_P, and goodness of fit χ^2 are 2.61%, 1.37%, and 0.08, respectively. The extracted lattice parameters a and c, and axis ratio c/a, decrease monotonically with increasing pressure, as shown in Fig. 1(b). Upon compression from 0.5 to 52.2 GPa, the parameters a and c decrease by 7.2% and 13.9%, respectively, revealing a large anisotropy of axial compressibility due to the quasi-two-dimensional nature of the lattice. Meanwhile, the overall volume decreases by 25.9%. Figure 1(c) shows the pressure (P) dependence of volume (V), which can be fitted by the third-order Birch-Murnaghan equation of state [26]: $P = \frac{3}{2}B_0[(V_0/V)^{\frac{7}{3}} - (V_0/V)^{\frac{5}{3}}]\{1 + \frac{3}{4}(B_0' - 4)[(V_0/V)^{\frac{2}{3}} - 1]\}$, where V_0, B_0, and B_0' are the volume, bulk modulus $-V/(dV/dP)$, and first-order derivative of the bulk modulus at zero pressure, respectively. The fitting yields $V_0 = 67.9 \pm 0.5$ Å^3, $B_0 = 53.3 \pm 7.4$ GPa, and $B_0' = 8.1 \pm 0.9$.

Raman spectroscopy is an effective and powerful tool in detecting lattice vibrations, which can provide information including electron-phonon coupling, weak lattice distortion, and/or structural transition. Bulk $NiTe_2$ displays a similar $1T$ structure of $TiTe_2$ and nine vibrational modes due to the same irreducible representation at the gamma point of the Brillouin zone [27]. Figure 2(a) shows the selective room-temperature Raman spectra of $NiTe_2$ single crystal at various pressures. At 0.6 GPa, one vibrational mode that can be assigned to the E_g mode is detected at ~84 cm^{-1} [13]. As illustrated in the inset of Fig. 2(b), the E_g mode involves in-plane atomic vibrations, with the top and bottom Te atoms moving in opposite directions [28]. In line with the stability of the pristine hexagonal phase as revealed by the XRD measurements, the E_g mode shifts gradually to higher frequencies without new peaks appearing with increasing pressure up to 35.7 GPa. Figures 2(b) and 2(c) display the pressure-dependent frequency and full width at half maximum (FWHM) obtained from Lorentz fittings of the E_g mode. With increasing pressure, one can see that the Raman frequency increases linearly but with different slopes below and above a critical pressure $P_c \sim 16$ GPa, as indicated by an arrow in Fig. 2(b). Similar to Refs. [29,30], the Grüneisen parameter $\gamma_i = (B_0/\omega_i) \times (d\omega_i/dP)$, with ω_i the ith phonon mode frequency, and B_0, the bulk modulus at zero pressure, is calculated for the E_g mode. Both the pressure coefficients and Grüneisen parameters before and after P_c are shown in Table S1 (see Supplemental Material [22]). Along with the change of pressure coefficient ($d\omega/dP$) from 2.07 to 0.99 cm^{-1} GPa^{-1}, the pressure-dependent FWHM exhibits a rather pronounced anomaly around P_c [see Fig. 2(c)]. As we know, the Raman linewidth

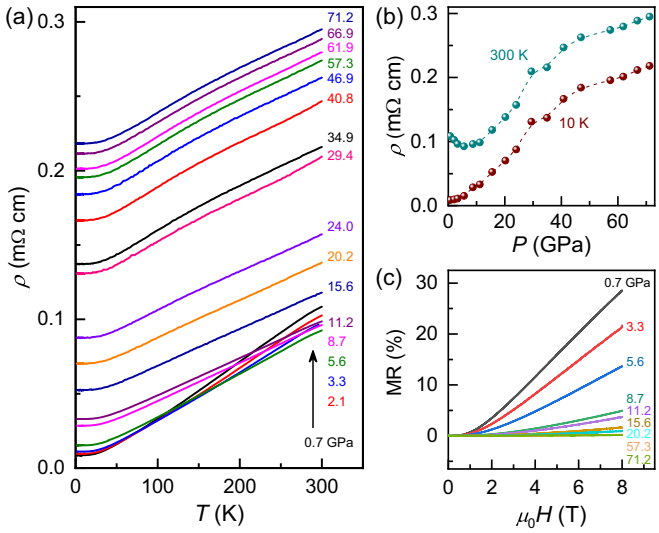

FIG. 3. (a) In-plane longitudinal resistivity curves $\rho(T)$ of $NiTe_2$ single crystal at various pressures up to 71.2 GPa. (b) Resistivity at 10 and 300 K as a function of pressure. (c) Representative magnetoresistance curves at 10 K under pressure.

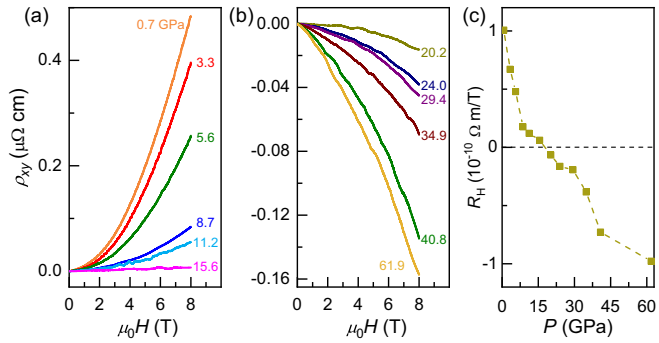

FIG. 4. (a,b) Pressure dependence of transversal Hall resistivity curves $\rho_{xy}(H)$ of $NiTe_2$ single crystal at 10 K. (c) Hall coefficient R_H as a function of pressure. The R_H is determined from the initial slope of $\rho_{xy}(H)$ at $H \to 0$.

is inversely proportional to the lifetime of the phonon mode, which involves information of not only phonon-phonon interactions but also the excitation-phonon interactions such as electron-phonon and spin-phonon coupling [31]. As the pressure increases, the linewidth of the phonon modes will generally increase. However, for the pressurized $NiTe_2$, the FWHM of the E_g mode exhibits an abrupt drop at pressures of 14.8–18.0 GPa. Without a structural transition occurring, the existence of anomalies in the phonon spectrum is reminiscent of a pressure-induced ETT or Lifshitz transition, which has been observed in some other transition metal chalcogenides, such as Bi_2Se_3 [32], Bi_2Te_3 [33], Sb_2Te_3 [34], Sb_2Se_3 [35], and $TiTe_2$ [27].

An ETT or Lifshitz transition occurs when an extreme of the electronic band structure crosses the Fermi energy level, which is associated to a van Hove singularity in the density of states [36]. Therefore, we further conducted high-pressure electrical resistivity measurements to search for possible evidence of the Lifshitz transition. Figure 3(a) shows the temperature-dependent resistivity $\rho(T)$ at various pressures. At 0.7 GPa, a metallic behavior is clearly presented in the temperature region from 1.8 to 300 K, similar to that at ambient condition [13]. The metallic behavior maintains with increasing pressure up to 71.2 GPa and no traces of superconductivity are detected down to 1.8 K. Note that the recent high-pressure experiments in polycrystalline $NiTe_2$ discover a superconducting transition without zero resistance between 12.0 and 54.5 GPa [37]. We also note that the possible impurities and defects are superconducting under pressure, such as element Te [38]. Meantime, the $\rho(T)$ curve is monotonically shifted upward except in the low-pressure region. The resistivity and magnetoresistance, $\mathrm{MR} = [(\rho(H) - \rho(0)]/\rho(0) \times 100\%$, at 10 K under various pressure are displayed in Figs. 3(b) and 3(c), respectively. Note that the resistivity of 300 K in Fig. 3(b) shows a minimum around 5 GPa. Since no structural phase transition occurs under high pressure and the structural parameter c/a concomitantly displays a slope change around 5 GPa (see Fig. 1), the anomaly around 5 GPa might be attributed to an ETT. The MR is almost completely suppressed at pressures above 15.6 GPa, but beyond that, no more anomalies associated with the Lifshitz transition can be discerned from Fig. 3.

High-pressure Hall resistivity measurements were further carried out to extract the evolution of charge carriers in the pressurized $NiTe_2$. Figures 4(a) and 4(b) show the selective Hall resistivity curves $\rho_{xy}(H)$ measured at 10 K under various pressures, where the magnetic field H is applied perpendicular to the ab plane. At 0.7 GPa, the $\rho_{xy}(H)$ curve exhibits a nonlinear feature with positive slope, indicating a hole-dominated multiband feature of the electrical transport in agreement with that at ambient pressure [39]. The Hall coefficient R_H, extracted from the slope of $\rho_{xy}(H)$ around zero field, decreases monotonically with increasing pressure and changes from positive to negative above 15.6 GPa [see Fig. 4(c)]. The sign change of the R_H demonstrates that the hole-dominated behavior maintains up to 15.6 GPa and transforms into electron-dominated behavior at higher pressures, which further evidences the change of the Fermi surface and could be viewed as a signature of the Lifshitz transition. We note that the temperature-induced Lifshitz transition in $ZrTe_5$ also involves the change of charge carrier type [40], which is very similar to our case.

In summary, we have systematically investigated the pressure effect on the structural and electronic properties of type-II Dirac semimetal $NiTe_2$ by combining synchrotron x-ray diffraction, Raman scattering, and electrical transport measurements. Although the x-ray diffraction results show the stability of pristine hexagonal structure up to 52.2 GPa, both pressure coefficient and linewidth of Raman mode E_g display abnormal behaviors across $P_c \sim 16$ GPa. Our findings unveil a pressure-induced Lifshitz transition of $NiTe_2$ at P_c, which is further supported by the change of charge carrier type through electrical transport analysis.

The authors are grateful for the financial support from the National Key Research and Development Program of China (Grants No. 2018YFA0305704 and No. 2016YFA0401804), the National Natural Science Foundation

of China (Grants No. U1632275, No. 11874362, No. U1932152, No. 11704387, No. 11804341, No. U1832209, No. 11804344, and No. 11605276), the Natural Science Foundation of Anhui Province (Grants No. 1808085MA06 and No. 1908085QA18), the Users with Excellence Project of Hefei Center CAS (Grant No. 2018HSC-UE012), and the Major Program of Development Foundation of Hefei Center for Physical Science and Technology (Grant No. 2018ZYFX002). Yonghui Zhou was supported by the Youth Innovation Promotion Association CAS (Grant No. 2020443). A portion of this work was supported by the High Magnetic Field Laboratory of Anhui Province. The x-ray experiments were performed at HPCAT (Sector 16, BM-D), Advanced Photon Source, Argonne National Laboratory. HPCAT operations are supported by DOE-NNSA under Award No. DE-NA0001974 and DOE-BES under Award No. DE-FG02-99ER45775, with partial instrumentation funding by NSF. The Advanced Photo Source is a U.S. Department of Energy (DOE) Office of Science by Argonne National Laboratory under Contract No. DE-AC02-06CH11357.

[1] A. H. Castro Neto, Phys. Rev. Lett. **86**, 4382 (2001).
[2] X. Qian, J. Liu, and L. Fu, Science **346**, 1344 (2014).
[3] Y. Qi, P. G. Naumov, M. N. Ali, C. R. Rajamathi, W. Schnelle, O. Barkalov, M. Hanfland, S. C. Wu, C. Shekhar, Y. Sun, V. Suss, M. Schmidt, U. Schwarz, E. Pippel, P. Werner, R. Hillebrand, T. Forster, E. Kampert, S. Parkin, R. J. Cava *et al.*, Nat. Commun. **7**, 11038 (2016).
[4] B. S. de Lima, R. R. de Cassia, F. B. Santos, L. E. Correa, T. W. Grant, A. L. R. Manesco, G. W. Martins, L. T. F. Eleno, M. S. Torikachvili, and A. J. S. Machado, Solid State Commun. **283**, 27 (2018).
[5] Q. H. Wang, K. Kalantar-Zadeh, A. Kis, J. N. Coleman, and M. S. Strano, Nat. Nanotechnol. **7**, 699 (2012).
[6] Y. Wu, D. Mou, N. H. Jo, K. Sun, L. Huang, S. L. Bud'ko, and P. C. Canfield, and A. Kaminski, Phys. Rev. B **94**, 121113(R) (2016).
[7] K. Deng, G. Wan, P. Deng, K. Zhang, S. Ding, E. Wang, M. Yan, H. Huang, H. Zhang, Z. Xu, J. Denlinger, A. Fedorov, H. Yang, W. Duan, H. Yao, Y. Wu, S. Fan, H. Zhang, X. Chen, and S. Zhou, Nat. Phys. **12**, 1105 (2016).
[8] K. Zhang, M. Yan, H. Zhang, H. Huang, M. Arita, Z. Sun, W. Duan, Y. Wu, and S. Zhou, Phys. Rev. B **96**, 125102 (2017).
[9] A. Sirohi, S. Das, P. Adhikary, R. R. Chowdhury, A. Vashist, Y. Singh, S. Gayen, T. Das, and G. Sheet, J. Phys.: Condens. Matter **31**, 085701 (2019).
[10] M. Yan, H. Huang, K. Zhang, E. Wang, W. Yao, K. Deng, G. Wan, H. Zhang, M. Arita, H. Yang, Z. Sun, H. Yao, Y. Wu, S. Fan, W. Duan, and S. Zhou, Nat. Commun. **8**, 257 (2017).
[11] W. Zheng, R. Schönemann, N. Aryal, Q. Zhou, D. Rhodes, Y. C. Chiu, K. W. Chen, E. Kampert, T. Förster, T. J. Martin, G. T. McCandless, J. Y. Chan, E. Manousakis, and L. Balicas, Phys. Rev. B **97**, 235154 (2018).
[12] Z. Huang, W. Zhang, and W. Zhang, Materials **9**, 716 (2016).
[13] C. Xu, B. Li, W. Jiao, W. Zhou, B. Qian, R. Sankar, N. D. Zhigadlo, Y. Qi, D. Qian, F.-C. Chou, and X. Xu, Chem. Mater. **30**, 4823 (2018).
[14] B. Ghosh, D. Mondal, C.-N. Kuo, C. S. Lue, J. Nayak, J. Fujii, I. Vobornik, A. Politano, and A. Agarwal, Phys. Rev. B **100**, 195134 (2019).
[15] H. J. Noh, J. Jeong, E. J. Cho, K. Kim, B. I. Min, and B. G. Park, Phys. Rev. Lett. **119**, 016401 (2017).
[16] H. Huang, S. Zhou, and W. Duan, Phys. Rev. B **94**, 121117(R) (2016).
[17] F. Zheng, X.-B. Li, Y. Lin, L. Xiong, and J. Feng, arXiv:1911.04668.
[18] Z. Chi, X. Chen, F. Yen, F. Peng, Y. Zhou, J. Zhu, Y. Zhang, X. Liu, C. Lin, S. Chu, Y. Li, J. Zhao, T. Kagayama, Y. Ma, and Z. Yang, Phys. Rev. Lett. **120**, 037002 (2018).
[19] X. C. Pan, X. Chen, H. Liu, Y. Feng, Z. Wei, Y. Zhou, Z. Chi, L. Pi, F. Yen, F. Song, X. Wan, Z. Yang, B. Wang, G. Wang, and Y. Zhang, Nat. Commun. **6**, 7805 (2015).
[20] D. Kang, Y. Zhou, W. Yi, C. Yang, J. Guo, Y. Shi, S. Zhang, Z. Wang, C. Zhang, S. Jiang, A. Li, K. Yang, Q. Wu, G. Zhang, L. Sun, and Z. Zhao, Nat. Commun. **6**, 7804 (2015).
[21] F. Liu, J. Li, K. Zhang, S. Peng, H. Huang, M. Yan, N. Li, Q. Zhang, S. Guo, X. Lü, P. Cai, L. Yin, S. Zhou, W. Duan, J. Shen, and W. Yang, Sci. China: Phys., Mech. Astron. **62**, 048211 (2018).
[22] See Supplemental Material at http://link.aps.org/supplemental/10.1103/PhysRevB.101.115124 for the experimental details and the supporting data; also see Refs. [23–25].
[23] C. Prescher and V. B. Prakapenka, High Pressure Res. **35**, 223 (2015).
[24] B. A. Hunter, RIETICAA Visual Rietveld Program, International Union of Crystallography Commission on Powder Diffraction Newsletter No. 20 (Summer 1998), http://www.rietica.org.
[25] H. K. Mao, J. Xu, and P. M. Bell, J. Geophys. Res. **91**, 4673 (1986).
[26] F. Birch, Phys. Rev. **71**, 809 (1947).
[27] V. Rajaji, U. Dutta, P. C. Sreeparvathy, S. C. Sarma, Y. A. Sorb, B. Joseph, S. Sahoo, S. C. Peter, V. Kanchana, and C. Narayana, Phys. Rev. B **97**, 085107 (2018).
[28] M. O'Brien, N. McEvoy, C. Motta, J.-Y. Zheng, N. C. Berner, J. Kotakoski, K. Elibol, T. J. Pennycook, J. C. Meyer, C. Yim, M. Abid, T. Hallam, J. F. Donegan, S. Sanvito, and G. S. Duesberg, 2D Mater. **3**, 021004 (2016).
[29] Y. A. Sorb, V. Rajaji, P. S. Malavi, U. Subbarao, P. Halappa, S. C. Peter, S. Karmakar, and C. Narayana, J. Phys.: Condens. Matter **28**, 015602 (2016).
[30] Y. A. Sorb, N. Subramanian, and T. R. Ravindran, J. Phys.: Condens. Matter **25**, 155401 (2013).
[31] M. Cardona, High Pressure Res. **24**, 17 (2004).
[32] R. Vilaplana, D. Santamaría-Pérez, O. Gomis, F. J. Manjón, J. González, A. Segura, A. Muñoz, P. Rodríguez-Hernández, E. Pérez-González, V. Marín-Borrás, V. Muñoz-Sanjose, C. Drasar, and V. Kucek, Phys. Rev. B **84**, 184110 (2011).

[33] R. Vilaplana, O. Gomis, F. J. Manjón, A. Segura, E. Pérez-González, P. Rodríguez-Hernández, A. Muñoz, J. González, V. Marín-Borrás, V. Muñoz-Sanjosé, C. Drasar, and V. Kucek, Phys. Rev. B **84**, 104112 (2011).

[34] O. Gomis, R. Vilaplana, F. J. Manjón, P. Rodríguez-Hernández, E. Pérez-González, A. Muñoz, V. Kucek, and C. Drasar, Phys. Rev. B **84**, 174305 (2011).

[35] A. Bera, K. Pal, D. V. S. Muthu, S. Sen, P. Guptasarma, U. V. Waghmare, and A. K. Sood, Phys. Rev. Lett. **110**, 107401 (2013).

[36] I. M. Lifshitz, Sov. Phys. JETP **11**, 1130 (1960).

[37] T. Li, K. Wang, C. Xu, Q. Hou, H. Wu, J.-Y. Ge, S. Cao, J. Zhang, W. Ren, X. Xu, N.-C. Yeh, B. Chen, and Z. Feng, arXiv:1911.07173.

[38] F. P. Bundy and K. J. Dunn, Phys. Rev. Lett. **44**, 1623 (1980).

[39] Q. Liu, F. Fei, B. Chen, X. Bo, B. Wei, S. Zhang, M. Zhang, F. Xie, M. Naveed, X. Wan, F. Song, and B. Wang, Phys. Rev. B **99**, 155119 (2019).

[40] H. Chi, C. Zhang, G. Gu, D. E. Kharzeev, X. Dai, and Q. Li, New J. Phys. **19**, 015005 (2017).